Understanding the Influence of Lattice Composition on the Photocatalytic Activity of Defect-Pyrochlore-Structured Semiconductor Mixed Oxides

*Larissa Schwertmann, Anna Grünert, Anna Pougin, Chenghua Sun, Michael Wark, and Roland Marschall**

The defect-pyrochlore-structured photocatalyst $CsTaWO_6$ is an ideal starting material for anion doping from the gas phase, and is known to be highly active for solar hydrogen generation under simulated sunlight without co-catalysts. To investigate the active site of $CsTaWO_6$ for hydrogen generation and to understand the effects of the two d^0 elements in the compound, systematic and successive element substitution of tantalum and tungsten on the crystallographic 16c sites of the starting material has been performed. Substituting lattice tantalum with niobium hardly changes the band gap of the resulting compounds $CsTa_{(1-x)}Nb_xWO_6$, but the photocatalytic activity for hydrogen generation and oxidation reactions is strongly influenced. By investigating the surface reactivity toward adsorption, surface effects altering the activity are identified. In contrast, substituting lattice tungsten with molybdenum reduces the band gap of $CsTaWO_6$ into the visible-light range. Materials containing Mo are however not able to generate hydrogen anymore, due to the altered conduction band positions proven by density functional theory calculations. $CsTaMoO_6$ exhibits a band gap of 2.9 eV and evolves oxygen efficiently under UV light irradiation after CoPi co-catalyst deposition, and even under visible light small amounts of oxygen.

1. Introduction

Solar energy conversion using photocatalytic or photoelectrochemical reactions to generate solar fuels has gained tremendous attention in the last decades with respect to a sustainable and clean future energy supply.[1–3] In particular, water splitting over semiconductor materials to generate hydrogen and oxygen from water using only solar light as energy source has been investigated extensively in the last years,[4–14] but the search for an ideal photocatalytic material or composite with high efficiency is still ongoing. Especially the search for efficient materials catalyzing the water oxidation half reaction is very demanding compared to the water reduction half reaction, since four electrons and four protons have to be released with the formation of an oxygen double bond. However, only with an efficient water oxidation half reaction, overall water splitting can be realized and optimized.

Since the reports by Boddy and Fujishima[15,16] about photoelectrochemical water oxidation and water splitting using TiO_2, many different oxide materials have been investigated for such reactions, including simple oxides like TiO_2, Ta_2O_5, Ga_2O_3, but also more complex mixed oxides like $NaTaO_3$, $SrTiO_3$, or Bi_2WO_6.[6] A promising material for hydrogen generation is $CsTaWO_6$, which crystallizes in defect-pyrochlore structure, and was first reported to be photocatalytically active under UV light (band gap E_g = 3.8 eV) in 2004.[17] Anion doping was recently investigated using nitrogen and/or sulfur to reduce its E_g into the visible-light range,[18–20] revealing that both the undoped and doped materials generate hydrogen under simulated sunlight without co-catalysts. Moreover, the doped materials were able to generate hydrogen in visible light, also without co-catalyst. The defect-pyrochlore structure turned out to be advantageous for homogeneous anion doping throughout the host material, which is important for efficient light absorption in visible light, but the active site for hydrogen generation without co-catalyst was not discussed.

Besides anion doping, the electronic structure of semiconductor photocatalysts can also be altered by cation doping[21,22] or by stoichiometric substitution of lattice-constructing elements. Concerning the latter case, Kudo and co-workers[23] showed already in 2002 that the E_g of $Sr_2Ta_2O_7$ can be engineered by substituting lattice tantalum (Ta) with niobium (Nb), reducing the E_g stepwise from 4.5 eV for $Sr_2Ta_2O_7$ down to 3.9 eV for $Sr_2Nb_2O_7$. It is also known that Bi_2WO_6 has an

L. Schwertmann, A. Grünert, A. Pougin,
Dr. M. Wark, Dr. R. Marschall
Ruhr-University Bochum
Laboratory of Industrial Chemistry
44801 Bochum, Germany
E-mail: roland.marschall@phys.chemie.uni-giessen.de
Dr. C. Sun
School of Chemistry
Monash University
Clayton Victoria 3800, Australia
Dr. M. Wark
Carl-von-Ossietzky University Oldenburg
Institute of Chemistry
26129 Oldenburg, Germany
Dr. R. Marschall
Justus-Liebig-University Giessen
Institute of Physical Chemistry
35392 Giessen, Germany

DOI: 10.1002/adfm.201403092

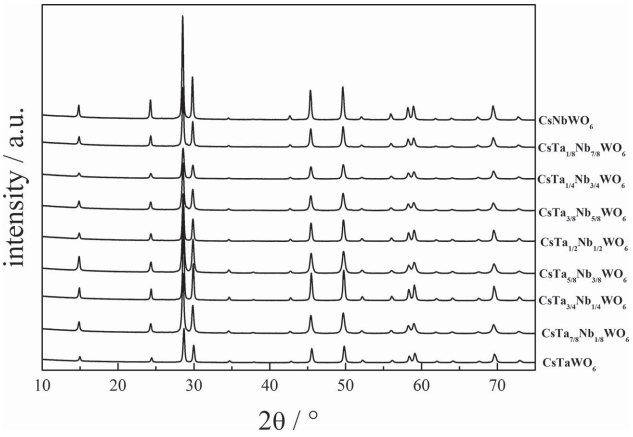

Figure 1. XRD patterns of $CsTa_{(1-x)}Nb_xWO_6$ materials.

E_g of ≈2.8 eV and the potential for water oxidation,[24,25] while the replacement of tungsten (W) with molybdenum (Mo) can lead to a monotonic decrease in E_g down to 2.36 eV.[26] In the case of Mo substitution, the degree of Mo 4d and W 5d orbitals forming the conduction band (CB) and the degree of delocalized excitation energy due to distortion of the crystal lattice were proposed to be responsible for the redshifted absorption.

With those reports in mind, to reveal the active site of $CsTaWO_6$ for hydrogen generation and to understand the effects of the two d^0 elements in the compound, we have performed systematic and successive element substitution of tantalum and tungsten on the crystallographic 16c sites of the starting material. Substituting lattice tantalum with niobium resulted in materials with the composition $CsTa_{(1-x)}Nb_xWO_6$, surprisingly showing hardly any change in band gap, but distinct differences in photocatalytic activity for oxidation and reduction reactions. Comparing $CsTaWO_6$ with $CsNbWO_6$ revealed differences in surface states, explaining the different photocatalytic activities by observing surface Lewis-base sites only on $CsTaWO_6$.

Substituting lattice tungsten with molybdenum resulted in materials with the composition $CsTaMo_xW_{(1-x)}O_6$, reducing the band gap into the visible-light range. To the best of our knowledge, there is only one report describing the synthesis of $CsTaMoO_6$ so far,[27] and no photocatalytic studies have been performed at all. Our materials containing Mo are however not able to generate hydrogen anymore, due to the altered CB positions proven by density functional theory (DFT) calculations, but evolve oxygen efficiently under UV light irradiation after CoPi cocatalyst deposition, and even oxygen under visible light.

2. Results and Discussion

2.1. Substitution of Ta with Nb

$CsTaWO_6$, $CsNbWO_6$, and the successive mixtures $CsTa_{(1-x)}Nb_xWO_6$ were prepared via solid state reaction (SSR) according to the literature,[18] by mixing stoichiometric amounts of Cs_2CO_3, Nb_2O_5, Ta_2O_5, and WO_3 and heating for 2 × 18 h at 810 °C with intermediate grinding. **Figure 1** shows the X-ray diffraction (XRD) patterns of the different materials after the synthesis.

Even with increasing amount of incorporated Nb, the patterns are nearly identical and in perfect agreement with previously reported diffraction data[17–19] and the standard diffraction patterns of $CsTaWO_6$ (JCPDS 25–0233) and $CsNbWO_6$ (JCPDS 25–0225). The similarity of the diffraction patterns indicates isostructural compounds, and the sharp and well-resolved reflections indicate highly crystalline materials, as expected after SSR. As known from the literature, the resulting defect-pyrochlore structure consists of randomly distributed, corner-sharing TaO_6 and WO_6 octahedra forming a 3D framework possessing tunnels with hexagonal cross-section down the *c*-axis, in which the Cs cations are located on the crystallographic 8b sites.[28] Upon incorporation of Nb, NbO_6 octahedra are also incorporated into the structure, but since Nb(V) and Ta(V) have the same effective ionic radius in octahedral configuration,[29] no shifts in the reflections can be observed. Moreover, no impurity phases are observed. Based upon Kubelka–Munk UV–Vis spectra measured in diffuse reflectance geometry and converted into Tauc plots, we have estimated the E_g for the different $CsTa_{(1-x)}Nb_xWO_6$ materials (**Figure 2**).

After complete substitution of Ta by Nb, the resulting E_g was surprisingly hardly shifted but being ≈3.7 eV for all the different compositions. This result is in contrast to commonly observed CB shifts reported for mixed oxide tantalates, like $Sr_2Ta_2O_7$ or $KSr_2Ta_5O_{15}$,[23,30] due to Nb 4d orbitals situated at more negative energies compared to Ta 5d orbitals contributing to the CB. Moreover, Ikeda et al.[17] reported a change in E_g by complete substitution of Ta for Nb in $CsTaWO_6$. However, their shift reported is less than 10 nm, and moreover by carefully analyzing the reported Kubelka–Munk spectra, E_g of ≈3.73 and 3.64 eV can be seen. Taken into account that estimation of band gaps from Kubelka–Munk spectra is usually slightly more inaccurate than from Tauc plots, we believe that our measured E_g values are accurately representing the optical transitions of our materials.

Photocatalytic hydrogen evolution experiments were performed for selected samples, and the photonic efficiencies are shown in **Figure 3**.

All the mixed metal oxides with defect-pyrochlore structure evolve hydrogen from methanol/water mixtures upon UV light

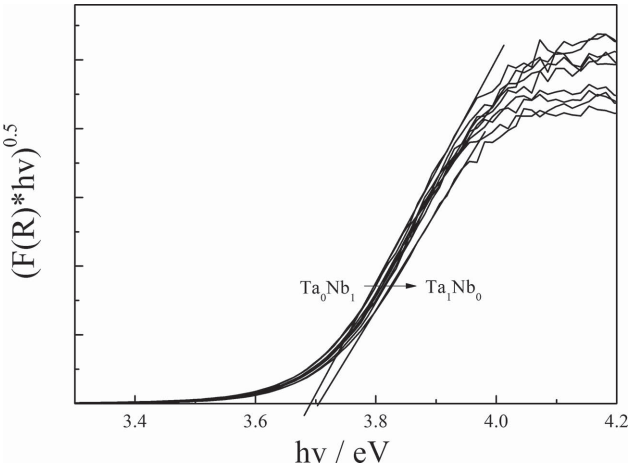

Figure 2. Tauc plots of $CsTa_{(1-x)}Nb_xWO_6$ materials.

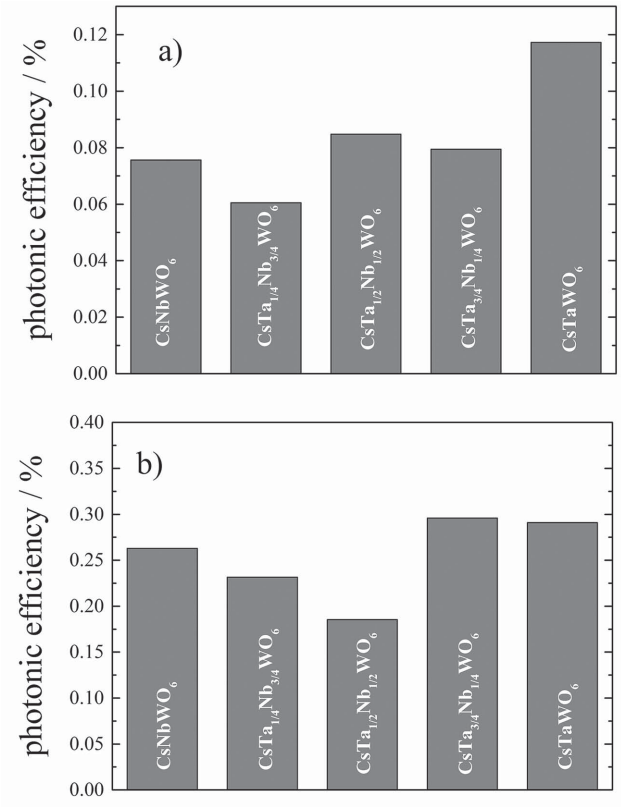

Figure 3. Photonic efficiencies for representative $CsTa_{(1-x)}Nb_xWO_6$ samples a) without cocatalyst or b) with 0.075 wt% Rhodium (Rh) photodeposited on the surface.

irradiation, indicating that active sites for hydrogen evolution are already present on the surface of these mixed metal oxides. However, while all the Nb-containing samples show comparable photonic efficiencies, Nb-free $CsTaWO_6$ shows 50% higher efficiency. Usually this is explained by the more negative CB positions, resulting in a larger driving force for photoexcited electrons to perform proton reduction. Actually, the band gaps are nearly identical (compare Figure 2); thus, the two CB positions should also be similar. Even if the CB positions would be slightly different, this would not result in such a distinct increase of the photonic efficiency by 50%. Upon photodeposition of Rh, the difference in efficiency of the $CsTa_{(1-x)}Nb_xWO_6$ defect pyrochlores is decreased. Photodeposited Rh acts as a cocatalyst withdrawing photoexcited electrons via Schottky contacts from the semiconductor CB, reducing the recombination probability of photogenerated electron–hole pairs which results in higher photonic efficiencies compared to unmodified samples.[31] As a result, the metallic Rh becomes the active site for hydrogen evolution at which protons are reduced to hydrogen. Without Rh, the active site for hydrogen evolution is not known.

The maximum efficiency was observed to be ≈0.3% for $CsTa_{3/4}Nb_{1/4}WO_6$ with a similar value for $CsTaWO_6$. The photonic efficiency for $CsNbWO_6$ is 0.27%, which is 1/10 lower compared to $CsTaWO_6$. By comparing the differences in efficiency with and without Rh, it seems that by Rh deposition photoexcited electrons are efficiently withdrawn from all the semiconductors. However, in the undecorated samples in the case of Nb-containing materials, the photoexcited electrons seem to have a higher recombination rate resulting in lower efficiencies compared to $CsTaWO_6$, which can be overcome by electron extraction to Rh. Moreover, it seems that less photoexcited electrons in unmodified $CsTaWO_6$ are recombining, resulting in the higher efficiency. This is still the case for Rh-decorated $CsTaWO_6$, but since Rh nanoparticle co-catalysts efficiently act as electron sinks, the recombination of charge carriers has less influence on the hydrogen evolution efficiency.

To further investigate the photocatalytic properties of mixed $CsTa_{(1-x)}Nb_xWO_6$ defect pyrochlores, we investigated the oxidation potential of photogenerated holes in the valence bands of the materials by terephthalic acid (TA) hydroxylation by OH radicals. Photogenerated holes can react with surface adsorbed water to generate highly reactive OH radicals which can be used to decompose, e.g., organic pollutants. These radicals can also react with TA to form 2-hydroxy terephthalic acid (TAOH), which emits a characteristic fluorescence at 426 nm.[18,19,32] By plotting the maxima at 426 nm evolving with time, the different compositions are compared in **Figure 4** for TA hydroxylation. The activity for OH radical formation and TA hydroxylation is highest for $CsNbWO_6$, while $CsTaWO_6$ in comparison shows only mediocre activity. The Ta–Nb mixture only gives rise to low activities. This result is unexpected since the valence band maximum of all the investigated materials should be positioned at the same potential, since it is constructed of O 2p orbitals. Although no difference in oxidation potential of photoexcited holes for OH radical formation is therefore expected, the activities are nevertheless very different. Moreover, the opposite trend in the materials activities is observed compared to hydrogen evolution. There, $CsTaWO_6$ was the most active material, but for TA hydroxylation $CsNbWO_6$ is the most active material.

Since the electronic structure of the different materials was shown to be very similar, we expected surface effects playing a major role in the photocatalytic performance of $CsTa_{(1-x)}Nb_xWO_6$. Therefore, we investigated the interaction of probe molecules CO_2 and NH_3 with the surface of $CsTaWO_6$ and $CsNbWO_6$ to reveal and identify surface sites affecting the catalytic activity, a common strategy known for metal

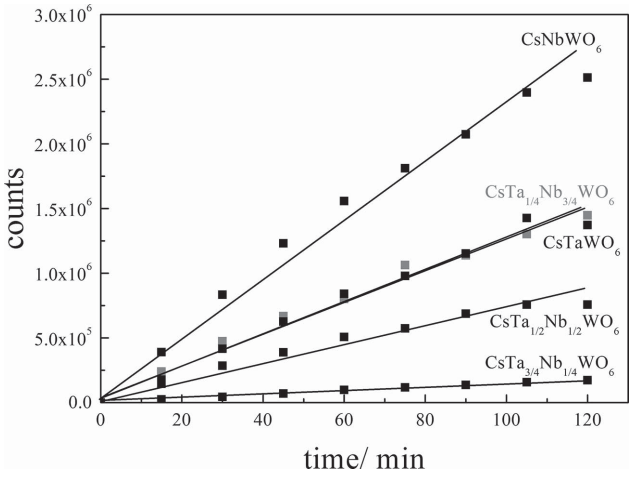

Figure 4. Maxima at 426 nm for TAOH production upon TA hydroxylation for different $CsTa_{(1-x)}Nb_xWO_6$ samples.

oxides.[33,34] NH_3 is a typical Lewis base due to its lone electron pair,[35] and can be used to detect Lewis-acid surface. On the other hand, CO_2 is acidic and can be used to detect basic sites in metal oxides.[33] For these measurements, samples were first heated in inert gas stream to remove any impurities from the surface, and cooled again to room temperature in inert gas flow. A reference infrared (IR) spectrum was then measured, followed by starting to dose probe gases for 15 min, measuring infrared (IR) spectroscopy in diffuse reflectance with 100 scans per second, a differential spectrum to detect any interactions with the sample surface. After 15 min, the gas flow was switched back to argon, investigating decreasing signals. As shown in Figure S1 (Supporting Information), neither $CsTaWO_6$ or $CsNbWO_6$ shows any interaction with ammonia besides a broad adsorption of surface hydroxyl groups (with features of N—H bands from acid–base interactions of ammonia with surface OH groups) and isolated hydroxyl groups (≈3600, ≈1600, ≈1200 cm^{-1}) from water in the measurement; thus, no Lewis-acid sites via interaction with metallic centers are present on the semiconductor surface. Figure S2 (Supporting Information) shows that $CsNbWO_6$ does not interact with CO_2. In contrast, $CsTaWO_6$ interacts with CO_2, as shown in **Figure 5**, revealing Lewis-base sites on the surface of this material.

For a better overview, only spectra after every 5 min are shown. In the first 15 min under CO_2 dosing, four very distinct bands between 1500 and 1800 cm^{-1} arise on the surface of $CsTaWO_6$, which are related to surface carbonates. In detail, since no literature data are available for carbonates on $CsTaWO_6$, those bands will be assigned according to TiO_2.[36] The band at 1733 cm^{-1} can thus be assigned to bridging carbonates on metal centers, bands at 1691 and 1657 cm^{-1} to bidentate carbonates, and the broad band at around 1610 cm^{-1} indicates carboxylate species on the surface. It can also be seen that the interaction is quite weak, since after switching to argon after 15 min the signals decrease immediately again, until only small amounts of carbonates remain present. The band at 1733 cm^{-1} moreover decreases faster than the others after purging with Ar again, also indicating bidentate species interacting weaker with the surface, thus being rinsed away faster than other species.

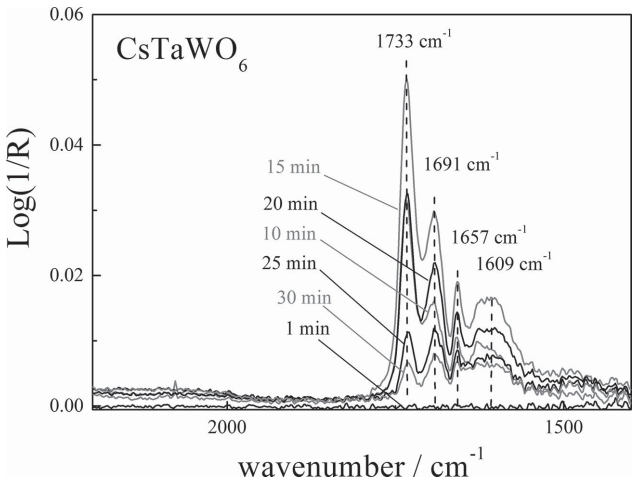

Figure 5. Diffuse reflectance IR spectra of $CsTaWO_6$ interacting with CO_2 dosed in the first 15 min, and then exchanged with argon flow.

As already mentioned, the interaction with CO_2 reveals Lewis-base sites on the photocatalyst surface. Such Lewis-base sites might be basic surface oxygen bridging two metal centers or basic O^{2-} ions exposed on the surface, both resulting in the observed carbonate species after forming a Lewis acid–base pair with acidic CO_2 and interaction with neighboring metal centers.[37] In aqueous environments, such centers can be consumed if not already hydroxylated in air, resulting in hydroxyl surface sites,[38] but still exhibiting free electron pairs and increased electron density. However, our investigation shows that $CsTaWO_6$ has a very different initial surface compared to $CsNbWO_6$.

The detected Lewis-base surface sites on $CsTaWO_6$, and the resulting hydroxylated surface in aqueous solution, can act as electron donors since they are centers of increased electron density, which react with photogenerated holes in the photoexcitation process. This might explain the different photocatalytic behavior of $CsTaWO_6$ and $CsNbWO_6$. After reaction of a photogenerated hole with basic surface sites, the hole is transferred onto surface oxygen (away from the photogenerated electron), and can be filled by the oxidation of methanol, which is a very fast reaction. This is a possible explanation why the photocatalytic activity of $CsTaWO_6$ for hydrogen generation without co-catalyst is higher than that for $CsNbWO_6$ (Figure 3a), which has no surface electron donor sites reacting with photogenerated holes. The whole process increases the lifetime of the photogenerated electrons in $CsTaWO_6$ compared to $CsNbWO_6$; in the latter, no Lewis-base sites can transfer the photogenerated hole to the surface, and thus the recombination of the photogenerated charges is more probable. Although the surface of both materials seems to be very different, $CsTaWO_6$ exhibiting recombination of photogenerated holes with basic surface sites, after Rh photodeposition this effect is negligible because electrons are efficiently transferred to Rh, resulting in spatially separated charges reducing the recombination probability.

2.2. Substitution of W with Mo

To investigate the influence of the second d^0 element in $CsTaWO_6$, we have prepared defect-pyrochlore-structured $CsTaMoO_6$ also by SSR using MoO_3 as Mo source. The resulting powder had a slight yellow color indicating a shift of the absorption edge into the visible-light range. Based upon Kubelka–Munk UV–Vis spectra measured in diffuse reflectance geometry and converted into Tauc plots, we have estimated the E_g for $CsTaWO_6$ being 3.6 eV (**Figure 6**). After complete substitution of W by Mo, the resulting E_g was estimated to 2.9 eV, showing a strong redshift in absorption. When W is only partly substituted with Mo, the E_g is also shifted according to Mo replacement, nearly monotonically as shown in Figure 6 and Figure S3 (Supporting Information). This is the first study of band gap engineering of this compound by lattice element substitution so far.

The distinct influence of Mo on the electronic structure of $CsTaWO_6$ can be demonstrated by DFT calculations. As shown in **Figure 7**, W and Mo mainly contribute to the CB of the respective solid, however also slightly to the valence band of the material.

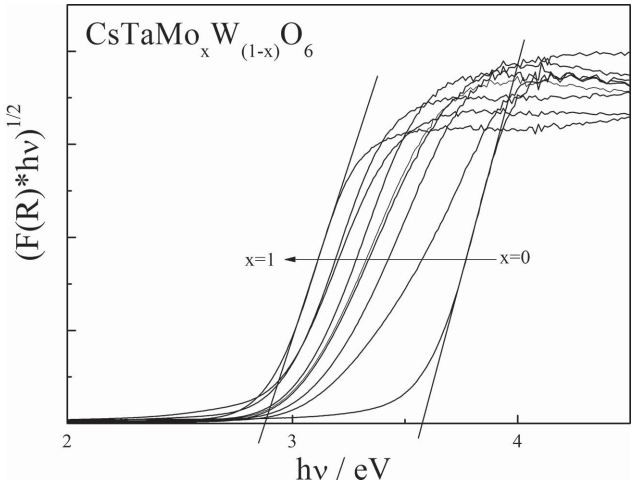

Figure 6. Tauc plots of $CsTaMo_xW_{(1-x)}O_6$ showing the decrease in E_g upon Mo substitution.

By using Mo, the CB edge is clearly shifted towards more negative values compared to $CsTaWO_6$, even lower than the proton reduction potential. Moreover, the valence band edge and the Fermi level (E_F) of $CsTaMoO_6$ do also shift, but not to the same extent, resulting in a narrowed E_g by Mo substitution. Estimated from the density of states (DOS), the E_g is reduced by ≈0.5 eV, down from ≈2.2 to ≈1.7 eV. Although DFT usually underestimates the E_g, the change in E_g is in good agreement with values taken from the Tauc plots (Figure 6). The overall shift of the conduction and valence band edges to more negative energies however has an important effect on the possible photocatalytic reactions, as will be shown later. We have additionally measured Mott–Schottky plots shown in Figure S4 (Supporting Information), the flat band potentials for $CsTaWO_6$ and $CsTaMoO_6$ being situated at ≈–0.7 and +0.1 V, respectively. The flat band potential is usually situated closely below the CB minimum for n-type semiconductors (both are n-type according to the slope of the curve), thus confirming the strong shift of the CB by Mo incorporation estimated from DFT calculations. The values are in good agreement with our DFT calculations, estimating a CB minimum of $CsTaMoO_6$ just below to the H^+/H_2 reduction potential. Since the flat band potential is usually not identical with the CB minimum, the DFT calculations were very accurate predicting the CB position of our material.

Figure 8 shows the XRD patterns for $CsTaWO_6$ and $CsTaMoO_6$ in comparison, both prepared by SSR. Both patterns are nearly identical and in perfect agreement with previously reported diffraction data[18,19,31] and the standard diffraction patterns of $CsTaWO_6$ (JCPDS 25–0233) and $CsTaMoO_6$ (JCPDS 49–0698). The similarity of the diffraction patterns again indicates isostructural compounds, and the sharp and well-resolved reflections indicate highly crystalline materials, as already observed in Section 2.1 for substitution with Nb.

In this case of MoO_6 octahedra forming the defect-pyrochlore framework with TaO_6, the reflections between 40° and 55° 2θ are slightly shifted to smaller angles 2θ. Mo has a slightly smaller effective ionic radius (59 pm) compared to W (60 pm) in octahedral coordination,[29] but the effective electronegativity of the 5d transition metal is lower than that of the 4d element, resulting in less covalent bonds with oxygen. The result is a modified crystal structure being the reason for the slight angle shifts.[26] A nearly continuous shift of the XRD patterns is observable with Mo incorporation (Figure S5, Supporting Information). In some cases of the mixed W–Mo materials, small amounts of unreacted impurity MoO_3 were observed. However, since no indication for MoO_3 is observed in absorption spectra, the amount must be very low. The morphology of the material is hardly changed, showing irregular-shaped particles (Figure S6, Supporting Information) similar to $CsTaWO_6$.[31]

Photocatalytic experiments for hydrogen and oxygen generation were first performed with UV light. As already reported in Section 2.1, $CsTaWO_6$ shows good performance for photocatalytic hydrogen generation from methanol/water mixtures, with and without rhodium (Rh) co-catalyst. However, incorporation of Mo results in hardly any hydrogen generated under UV light irradiation of a suspension of $CsTaMo_xW_{(1-x)}O_6$ ($0.125 \leq x \leq 1$). The explanation for this behavior can be found in the changed electronic structure of the defect-pyrochlore materials upon Mo incorporation. As followed from DFT calculations and Mott–Schottky results, not only is the E_g reduced by Mo incorporation, but also the band edge potentials are changed. Thus, the CB minimum of Mo incorporated samples is positioned lower than the water reduction potential (shown in Figure 7 is the potential for proton reduction in vacuum), resulting in the inability of hydrogen generation.

In contrast, $CsTaMoO_6$ is highly capable of photocatalytic oxygen evolution. First, photocatalytic experiments have been performed under UV light irradiation to investigate optimum co-catalysts for the oxygen

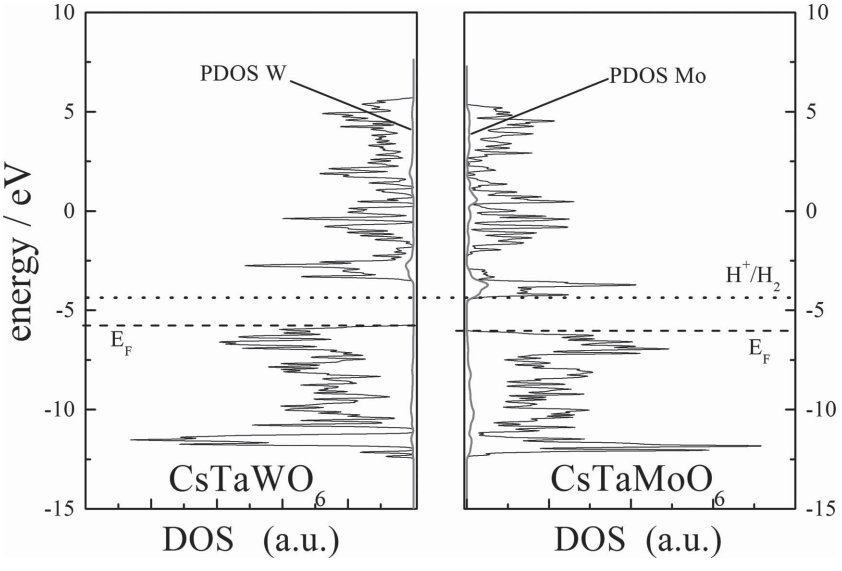

Figure 7. Density of states (DOS) of $CsTaWO_6$ (left) and $CsTaMoO_6$ (right), together with partial DOS of W and Mo (for only one atom, respectively).

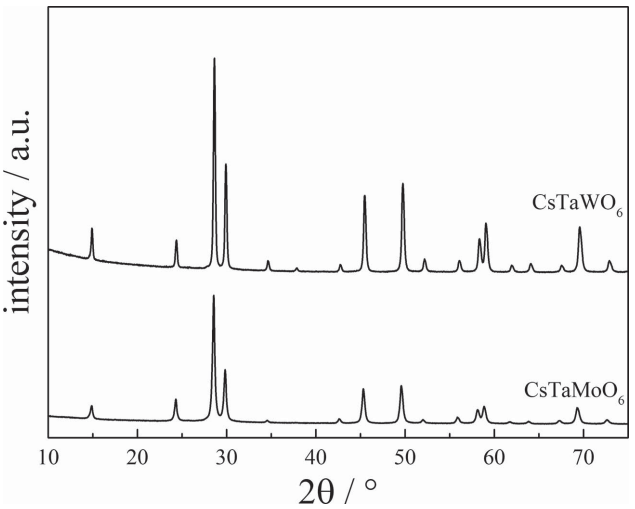

Figure 8. XRD patterns of $CsTaWO_6$ and $CsTaMoO_6$.

evolution, and optimum amounts of co-catalyst. As shown in **Figure 9**, different amounts of IrO_2 and CoPi[39] were tested in the presence of sodium iodate ($NaIO_3$).[40]

CoPi is clearly the more active co-catalyst in combination with $CsTaMoO_6$. More than 2.75% efficiency for oxygen evolution was achieved by using the optimum amount of only 0.25 wt% (calculated on basis of Co) of CoPi after photodeposition. With 0.5 wt% IrO_2 however only 1.5% photonic efficiency was reached. Figure 9 also shows that with increasing amount of CoPi, the oxygen evolution efficiency slightly decreases. The reason might be the increasing size of CoPi clusters formed after photodeposition, having a slightly reduced active surface area with increasing size, and thus resulting in a decreased reaction rate. Comparable amounts of CoPi were also deposited on $CsTaWO_6$ and $CsNbWO_6$ for comparison and, as expected, $CsTaMoO_6$ is far more active for oxygen evolution due to the reduced band gap and thus more photons are absorbed for

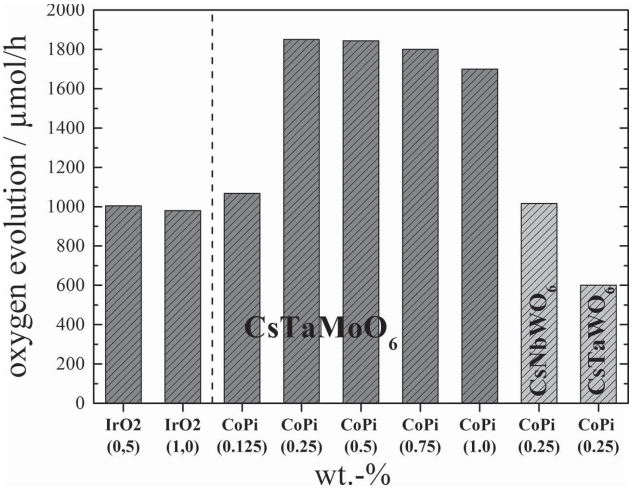

Figure 9. Photonic efficiencies for oxygen evolution with UV light irradiation of $CsTaMoO_6$, after photodeposition of different amounts of IrO_2 or CoPi, compared to $CsTaWO_6$ and $CsNbWO_6$.

charge carrier generation. Moreover, $CsNbWO_6$ is more active in oxygen evolution than $CsTaWO_6$, which might be due to the already investigated Lewis-base surface sites on $CsTaWO_6$. Lewis-base surface sites have a high electron density, which can have a repulsive effect on the sacrificial electron acceptor IO_3^-. Thus, photoexcited electrons cannot react with the sacrificial agent, and recombine with holes, resulting in lower activities for oxygen evolution. In addition, the surface could also be blocked over time with adsorbed sodium.

$CsTaMoO_6$ also shows the absence of any surface Lewis-base sites, as detected via IR spectroscopy during CO_2 interaction (Figure S7, Supporting Information); thus, all photogenerated holes are available for water oxidation.

We have also measured oxygen evolution under the same conditions for all three different materials, but without co-catalyst. As can be seen in Figure S8 (Supporting Information), all three defect pyrochlores evolve oxygen without any co-catalyst with the photonic efficiency given. The nature of the active site for oxygen evolution without CoPi is however not clear. The efficiencies are lower compared to the CoPi-modified samples, and the differences are also less pronounced. This might indicate that the oxidation of water on the pure photocatalysts is very slow, even with sacrificial agents, and charge carriers recombine fast resulting in comparable activities. $CsTaMoO_6$ shows slightly higher activity due to more photons absorbed, and $CsNbWO_6$ is again slightly more active than $CsTaWO_6$.

Finally, we investigated photocatalytic oxygen evolution of CoPi-modified $CsTaMoO_6$ under visible light. Therefore, we used 2 M $NaNO_2$ solution to cut off the UV wavelengths of our Hg mid-pressure immersion lamp for visible-light irradiation.[41–43] Compared to the high efficiency for oxygen evolution upon UV light irradiation, CoPi-modified $CsTaMoO_6$ generates only around 10 µmol h^{-1} oxygen in the presence of $NaIO_3$ (ξ = 0.015%). Stepwise substitution of lattice W by Mo led to a substantial redshift of the absorption with Mo introduction, as shown in Figure 6. Although this effect is very apparent reducing the E_g by about 0.65 eV, the E_g could not be reduced below 2.9 eV in this material system upon Mo introduction. Thus, only a small part of the visible-light emission from the used and filtered Hg lamp can be used to generate charge carriers in $CsTaMoO_6$ for photocatalytic reactions, resulting in the comparatively low efficiency for oxygen evolution. However, under UV light irradiation, oxygen evolution is very effective, showing that $CsTaMoO_6$ is in principle highly capable of oxygen evolution. Investigations with simulated sunlight will give further details about the capabilities of $CsTaMoO_6$ producing oxygen. The combination with an effective visible-light absorbing H_2-evolving photocatalyst will be investigated in the future to lead to a highly effective Z-scheme[44] photocatalyst system utilizing CoPi-modified $CsTaMoO_6$ for visible-light overall water splitting.

3. Conclusion

Lattice variations of defect-pyrochlore-structured $CsTaWO_6$ have profound effects on its photocatalytic activity, which were investigated with respect to hydrogen evolution, TA hydroxylation, and oxygen evolution.

Successive substitution of Ta with Nb hardly changes the electronic structure of the photocatalyst; measured optical band gaps of all prepared $CsTa_{(1-x)}Nb_xWO_6$ materials show similar values. However, the photocatalytic activity is strongly influenced by effects due to Lewis-base surface sites on $CsTaWO_6$ identified by CO_2 adsorption and IR spectroscopy, which are not present on $CsNbWO_6$ or $CsTaMoO_6$. As a result, $CsTaWO_6$ is more active for hydrogen generation, while $CsNbWO_6$ is more active for oxidation reactions.

We also presented the preparation and characterization of the novel photocatalyst $CsTaMo_xW_{(1-x)}O_6$ for photocatalytic oxygen evolution. Band gap engineering of this defect-pyrochlore-structured material has been investigated for the first time via substitution of lattice W by Mo starting from the well-known $CsTaWO_6$ material. The photocatalytic activities for hydrogen or oxygen evolution have been investigated, showing that $CsTaMoO_6$ is not able to generate hydrogen due to its too positive CB minimum, but evolves high amounts of oxygen under UV light irradiation after CoPi cocatalyst deposition, and even under visible light small amounts of oxygen. This strategy can be easily applied to other tungstate materials to avoid post-synthetic doping processes for band gap engineering achieving visible-light absorption.

4. Experimental Section

Preparation of Materials: Defect-pyrochlore-structured materials were prepared by SSR. Stoichiometric amounts of cesium carbonate (Cs_2CO_3, Aldrich), tantalum oxide (Ta_2O_5, Aldrich), niobium oxide (Nb_2O_5, Aldrich), tungsten oxide (WO_3, Alfa Aesar), and molybdenum oxide (MoO_3, Aldrich) were mixed vigorously in a mortar and calcined at 1073 K for 36 h (973 K for Mo-containing samples), with one intermediate grinding after 18 h. Co-catalyst photodeposition was performed in a home-made closed gas evolution system under inert gas atmosphere. For CoPi deposition, 700 mg photocatalyst was suspended in 600 mL aqueous 0.1 M potassium phosphate buffer solution (pH 7) including given amounts of cobalt nitrate ($Co(NO_3)_2$ (Alfa Aesar), and irradiated with a 700 W Hg mid-pressure immersion lamp (set to 500 W) for 5 h. Subsequently, the photocatalysts were filtered off, washed, and dried at room temperature before use in photocatalytic experiments. For photodeposition of 0.075 wt% Rh, Na_3RhCl_6 (Aldrich) was used as precursor in an 8% methanol/water mixture instead, in which hydrogen evolution experiments were also performed. Prior to the photodeposition reactions, the whole system, with the photocatalyst and precursors included, was flushed with argon 6.0 at 200 NmL min^{-1} for ≈30 min to remove any trace of air. For IrO_2, $Na_3[IrCl_6]$ was used as a precursor in the presence of 3×10^{-3} M $NaNO_3$ solution.[45]

Characterization: XRD patterns were recorded on a PANalytical MPD diffractometer using CuKα radiation (λ = 1.5406 Å) in the range of 10° to 75° 2θ. UV–Vis diffuse reflectance spectra were measured using a PerkinElmer Lambda 650 UV–Vis spectrometer equipped with a Praying Mantis mirror unit. The obtained spectra were converted by the Kubelka–Munk function, F(R), into absorption spectra, using $BaSO_4$ as a white standard. Optical band gaps (E_g) were obtained via Tauc-plot method according to previous reports.[31]

Computational Details: $CsTaWO_6$ and $CsTaMoO_6$ were modeled by a model shown in Figure S9 (Supporting Information), in which Ta/W and Ta/Mo ratio is 1:1. The structures were fully relaxed with the maximum force less than 0.05 eV $Å^{-1}$, followed by further calculation of electronic structures. All calculations were carried out under the framework of DFT within the generalized gradient approximation,[46] together with the use of Perdew–Burke–Ernzerhof functional,[47] which has been implemented in the DMol3 code[48] with the employment of double numeric quality basis with a global orbital cutoff of 4.5 Å. The k-space is sampled by the gamma point. No significant difference was observed when more k-points were employed (e.g., with a Monkhorst–Pack mesh of $3 \times 3 \times 3$).

Photocatalytic Experiments: Photocatalytic hydrogen and oxygen evolution was investigated with a home-built, air-free closed gas system using a typical double-walled inner irradiation-type quartz reactor described earlier.[31] As a light source, a 700 W Hg mid-pressure immersion lamp (Peschl UV-Consulting, set to 72% power = 500 W) was used for irradiation and cooled to 10 °C with a double-walled quartz mantle using a thermostat (LAUDA). Gas evolution was measured online using a multichannel analyzer (Emerson) equipped with detectors for the determination of the concentration of hydrogen (thermal conductivity detector), oxygen (paramagnetism), and carbon dioxide (IR). Argon 6.0 was used as carrier gas; the continuous gas flow was controlled by a 200 NmL min^{-1} Bronkhorst mass flow controller. The gas flow was set to 50 N mL min^{-1}. All reactions were performed at 13 °C. 400 mg of photocatalyst was suspended in 600 mL water including 8 vol% methanol or 3×10^{-3} M $NaIO_3$, respectively. Before photocatalytic reactions were initiated, the whole system, with the photocatalyst included, was flushed with argon 6.0 at 200 NmL min^{-1} for ≈30 min to remove any trace of air. Measurements were repeated several times; the error is <10 µmol h^{-1}. Photonic efficiencies were calculated with a photon flux of 2.64×10^5 mol h^{-1} (assuming a mean quantum yield of 1.2) for the used 500 W Hg lamp, determined with ferrioxalate actinometry.[49] For O_2 evolution, the following equation was used:

$$\xi = \frac{O_2 \text{ evolution rate [mol/h]} \times 4 \times 100}{\text{photon flux [mol/h]}} \quad (1)$$

For H_2 evolution, photocurrent doubling with MeOH was expected, meaning that one photon results in two electrons due to formed hydroxymethyl radicals injecting one electron into the CB of our photocatalysts.[50] Thus, photonic efficiencies were calculated by

$$\xi = \frac{H_2 \text{ evolution rate [mol/h]} \times 100}{\text{photon flux [mol/h]}} \quad (2)$$

Supporting Information

Supporting Information is available from the Wiley Online Library or from the author.

Acknowledgements

The authors thank Lina Freitag (Ruhr-University Bochum) for CO_2 and NH_3 adsorption investigations, Dr. Thomas Reinecke (Ruhr-University Bochum) for XRD measurements, and Stefan Schünemann (Ruhr-University Bochum) for ferrioxalate actinometry experiments. The authors would also like to thank Prof. Martin Muhler (Ruhr-University Bochum) for his support. The project "Sustainable Chemical Synthesis" (SusChemSys) is co-financed by the European Regional Development Fund (ERDF) and the state of North Rhine-Westphalia, Germany, under the Operational Program "Regional Competitiveness and Employment" 2007–2013. R.M. gratefully acknowledges funding in the Emmy-Noether program (MA 5392/3–1) of the German Research Foundation DFG, and funding by the Mercator Research Center Ruhr (MERCUR, An-2012–0068).

Received: September 8, 2014
Revised: November 25, 2014
Published online: December 22, 2014

[1] N. S. Lewis, *Nature* **2001**, *414*, 589.
[2] N. S. Lewis, D. G. Nocera, *Proc. Natl. Acad. Sci. U.S.A.* **2006**, *103*, 15729.
[3] T. Faunce, S. Styring, M. R. Wasielewski, G. W. Brudvig, A. W. Rutherford, J. Messinger, A. F. Lee, C. L. Hill, H. deGroot, M. Fontecave, D. R. MacFarlane, B. Hankamer, D. G. Nocera,

D. M. Tiede, H. Dau, W. Hillier, L. Wang, R. Amal, *Energy Environ. Sci.* **2013**, *6*, 1074.
[4] F. E. Osterloh, *Chem. Mater.* **2007**, *20*, 35.
[5] A. Kudo, Y. Miseki, *Chem. Soc. Rev.* **2009**, *38*, 253.
[6] X. Chen, S. Shen, L. Guo, S. S. Mao, *Chem. Rev.* **2010**, *110*, 6503.
[7] W. Y. Teoh, J. A. Scott, R. Amal, *J. Phys. Chem Lett.* **2012**, *3*, 629.
[8] P. D. Tran, L. H. Wong, J. Barber, J. S. C. Loo, *Energy Environ. Sci.* **2012**, *5*, 5902.
[9] F. E. Osterloh, *Chem. Soc. Rev.* **2013**, *42*, 2294.
[10] Y. Horiuchi, T. Toyao, M. Takeuchi, M. Matsuoka, M. Anpo, *Phys. Chem. Chem. Phys.* **2013**, *15*, 13243.
[11] X. Zong, L. Wang, *J. Photochem. Photobiol. C* **2014**, *18*, 32.
[12] R. Marschall, L. Wang, *Catal. Today* **2014**, *125*, 111.
[13] R. Marschall, *Adv. Funct. Mater.* **2014**, *24*, 2421.
[14] F. Fresno, R. Rortela, S. Suárez, J. M. Coronado, *J. Mater. Chem. A* **2014**, *2*, 2863.
[15] P. J. Boddy, *J. Electrochem. Soc.* **1968**, *115*, 199.
[16] A. Fujishima, K. Honda, *Nature* **1972**, *238*, 37.
[17] S. Ikeda, T. Itani, K. Nango, M. Matsumura, *Catal. Lett.* **2004**, *98*, 229.
[18] A. Mukherji, R. Marschall, A. Tanksale, C. Sun, S. C. Smith, G. Q. Lu, L. Wang, *Adv. Funct. Mater.* **2011**, *21*, 126.
[19] R. Marschall, A. Mukherji, A. Tanksale, C. Sun, S. C. Smith, L. Wang, G. Q. Lu, *J. Mater. Chem.* **2011**, *21*, 8871.
[20] J. Sun, X. Zhao, H. Sun, W. Fan, *J. Solid State Chem.* **2012**, *194*, 352.
[21] W. Choi, A. Termin, M. R. Hoffmann, *J. Phys. Chem.* **1994**, *98*, 13669.
[22] J. Z. Bloh, R. Dillert, D. W. Bahnemann, *J. Phys. Chem. C* **2012**, *116*, 25558.
[23] M. Yoshino, M. Kakihana, W. S. Cho, H. Kato, A. Kudo, *Chem. Mater.* **2002**, *14*, 3369.
[24] F. Amano, A. Yamakata, K. Nogami, M. Osawa, B. Ohtani, *J. Am. Chem. Soc.* **2008**, *130*, 17650.
[25] J. C. Hill, K.-S. Choi, *J. Mater. Chem. A* **2013**, *1*, 5006.
[26] L. Zhang, Y. Man, Y. Zhu, *ACS Catal.* **2011**, *1*, 841.
[27] T. Kar, R. N. P. Choudhary, *Mater. Sci. Eng. B* **2002**, *90*, 224.
[28] A. V. Knyazev, N. G. Chernorukov, N. N. Smirnova, N. Yu. Kuznetsova, A. V. Markin, *Thermochim. Acta* **2008**, *470*, 47.
[29] R. D. Shannon, *Acta Cryst.* **1976**, *A32*, 751.
[30] P. Wang, L. Schwertmann, R. Marschall, M. Wark, *J. Mater. Chem. A* **2014**, *2*, 8815.
[31] L. Schwertmann, M. Wark, R. Marschall, *RSC Adv.* **2013**, *3*, 18908.
[32] G. Liu, L. Wang, C. Sun, X. Yan, X. Wang, Z. Chen, S. C. Smith, H. M. Cheng, G. Q. Lu, *Chem. Mater.* **2009**, *21*, 1266.
[33] J. C. Lavalley, *Catal. Today* **1996**, *27*, 377.
[34] H. Knözinger, S. Huber, *J. Chem. Soc., Faraday Trans.* **1998**, *94*, 2047.
[35] G. N. Lewis, *Valence and the Structure of Atoms and Molecules*, The Chemical Catalog Company, New York **1923**.
[36] A. M. Turek, I. E. Wachs, E. DeCanio, *J. Phys. Chem.* **1992**, *96*, 5000.
[37] G. Martra, *Appl. Catal. A* **2000**, *200*, 275.
[38] L. Mino, G. Spoto, A. M. Ferrari, *J. Phys. Chem. C* **2014**, *118*, 25016.
[39] M. W. Kanan, D. G. Nocera, *Science* **2008**, *321*, 1072.
[40] D. Wang, R. Li, J. Zhu, J. Shi, J. Han, X. Zong, C. Li, *J. Phys. Chem. C* **2012**, *116*, 5082.
[41] K. Maeda, T. Takata, M. Hara, N. Saito, Y. Inoue, H. Kobayashi, K. Domen, *J. Am. Chem. Soc.* **2005**, *127*, 8286.
[42] D. Lu, T. Takata, N. Saito, Y. Inoue, K. Domen, *Nature* **2006**, *440*, 295.
[43] K. Maeda, K. Teramura, N. Saito, Y. Inoue, K. Domen, *J. Catal.* **2006**, *243*, 303.
[44] K. Maeda, *ACS Catal.* **2013**, *3*, 1486.
[45] A. Iwase, H. Kato, A. Kudo, *Chem. Lett.* **2005**, *34*, 946.
[46] W. Kohn, L. Sham, *J. Phys. Rev.* **1965**, *140*, 1133.
[47] J. P. Perdew, K. Burke, M. Ernzerhof, *Phys. Rev. Lett.* **1996**, *77*, 3865.
[48] B. Delley, *J. Chem. Phys.* **2000**, *113*, 7756.
[49] C. G. Hatchard, C. A. Parker, *Proc. R. Soc. Math. Phys. Eng. Sci.* **1956**, *235*, 518.
[50] Y. K. Kho, A. Iwase, W. Y. Teoh, L. Mädler, A. Kudo, R. Amal, *J. Phys. Chem. C* **2010**, *114*, 2821.